A Simulation Framework for Precision Landing and Hazard Avoidance Technology Assessments

Alicia Dwyer Cianciolo,[1] Soumyo Dutta,[2] Rafael Lugo, [3]
Anthony Williams[4]
NASA Langley Research Center, Hampton, Virginia, 23681, USA

Po-Ting Chen[5]
Jet Propulsion Laboratory, Pasadena CA, USA

To meet NASA's challenge to return humans to the Moon in 2024 and establish a sustainable presence in 2028 requires advances in autonomous spacecraft navigation. The Safe and Precise Landing Integrated Capabilities Evolution (SPLICE) project, which leverages previous work at NASA to develop multi-mission precision landing and hazard avoidance technologies, is using a multi-faceted approach to achieve the advanced landing requirements. In addition to increasing the technology readiness level of key sensors and developing high performance space computing, SPLICE uses simulations to determine navigation requirements and evaluate sensor performance. The effort evaluates various precision landing concepts of operations, not only for the lunar human and robotic missions, but also for potential missions to other solar system destinations. This paper summarizes the six degree-of-freedom high fidelity simulation framework, trajectory design methodology, and sensor models being considered for a variety of precision lander missions. Initial results of the navigation sensor performance for a human Mars mission are presented. Finally, trade and sensitivity studies are outlined for future work to fully characterize sensor performance assumptions and modifications required to achieve precision landing and hazard avoidance.

I. Introduction

NASA's challenge to return humans to the Moon in 2024 and establish a sustainable presence in 2028 requires advances in autonomous spacecraft navigation. The Safe and Precise Landing Integrated Capabilities Evolution (SPLICE) project, which leverages previous work at NASA to develop multi-mission precision landing and hazard avoidance (PL&HA) technologies, is using a multi-faceted approach to achieve the advanced landing requirements. In addition to increasing the technology readiness level of key sensors and developing high performance space computing, SPLICE uses various simulation capabilities to determine navigation requirements and evaluate potential navigation sensor performance. This effort evaluates various precision landing concepts of operations, not only for the lunar human and robotic missions to the equator and poles of the moon, but also for potential missions to other solar system destinations. Other precision lander missions include both large robotic and human class missions to Mars, as well as robotic missions to Europa [1]. Therefore, this paper summarizes the six degree-of-freedom high fidelity simulation framework developed over the past two years to support multiple mission concepts. Key aspects

[1] Aerospace Engineer, Atmospheric Flight and Entry Systems Branch, AIAA Senior Member.
[2] Aerospace Engineer, Atmospheric Flight and Entry Systems Branch, AIAA Senior Member.
[3] Aerospace Engineer, Atmospheric Flight and Entry Systems Branch, AIAA Member.
[4] Research Computer Scientist, Atmospheric Flight and Entry Systems Branch.
[5] Member of Technical Staff, Guidance and Control Section

of the framework are code modularity, model input standardization, and multiple parameter guidance optimization. These features allow for rapid model implementation and make the simulation flexible to accommodate various concepts of operations. Additionally, sensor models are also parameterized to enable sensor quality evaluation. For example, sensor quantities like noise, bias, internal and external alignment errors, and scale factors can all be modified to reflect increases in quality, complexity, and cost. Using a consistent trajectory design methodology, sensor models can be evaluated and compared across a variety of precision lander missions. The ultimate goal of the task it to identify sensor or sensor suite commonalities that exist for many different concepts of operations. Those sensor suites become technology investment recommendations for near-term and long-term missions.

The concept of operations considered here is the Entry, Descent and Landing (EDL) of a low lift-to-drag vehicle delivering 20t payload to the surface of Mars and is described in Section II. Section III describes the high-fidelity simulation and models specifications assumed. Initial results of the navigation sensor performance are presented in Section IV. Finally, in Section V, trade and sensitivity studies are outlined for future work to characterize sensor performance assumptions and modifications required to achieve precision landing and hazard avoidance at Mars and other destinations.

II. Mission Concept of Operations and Ground Rules

The entry vehicle considered for this study includes a 16 m diameter inflatable deployable aeroshell, or heat shield, attached to a common lander system. The notional human Mars mission architecture assumes that three to four landers are delivered to the same landing zone. Cargo elements including power, rovers, ascent vehicle, and logistics are delivered prior to the crew. Finally, the crew arrives in the habitat. Each lander is delivered to a parking orbit either by aerocapture or an in-space transfer stage. This study considers a one-sol parking orbit (33,800 km x 250 km). The concept of operations initiates at the apoapsis of a parking orbit where the vehicle performs an instantaneous deorbit burn using the reaction control system (RCS). During deorbit, the vehicle again uses RCS to reorient prior to entry such that it enters the atmosphere with an angle of attack of -6 deg. The vehicle flies with a lift-to-drag ratio near 0.2 and a ballistic coefficient of 140 kg/m^2. At a sensed deceleration of 0.2 Earth G's, the vehicle activates the numerical predictor corrector (NPC) guidance algorithm. The NPC uses DFC to influence the flight trajectory. Trajectory control during entry is achieved using four aerodynamic flaps, each one rate-limited to 18°/s. These flaps are used to implement a direct force control (DFC). The algorithm finds the optimal flap settings to control both angle of attack and slide slip to minimize state errors at engine initiation by modulate angle of attack to manage downrange errors and angle of sideslip to manage crossrange errors. Roll control is achieved using RCS with a minimum on/off time of 0.01 s. The guidance algorithm determines when to start eight 100 kN engines based on both inertial and relative sensor information so that the vehicle lands at 0 km above the reference Mars Orbiter Laser Altimeter areoid near the equator. For the powered descent phase, the NPC guidance commands the throttle setting of each of the eight lander engines to achieve an augmented gravity turn, which allows for small changes in angle of attack (<5deg) in order to reach the target. The nominal powered descent trajectory is designed with the eight engines throttled at 80% to leave margin for differential throttling for attitude control, trajectory dispersions, increases in vehicle design mass, etc. Further description of guidance is given in section III.A. An image of the reference vehicle and concept of operations including the surface operations to stow the inflatable structure are shown in Fig. 1 [2]. The figure includes quantities at critical events during the nominal trajectory. This human Mars concept is one of many being considered for the SPLICE sensor evaluation effort [1].

Multiple landers delivered to a single landing zone and the desire to minimize the distance to previously landed assets drive the precision landing requirements. Analysis has shown that the size of engine thrust, engine cant angle and throttle down profile being assumed for the human scale vehicle may distribute regolith up to 700 m on the surface Mars [3]. Therefore, a keep out zone is established that prevents any lander from landing closer than one km from a previously landed asset. To minimize the distance between assets then, a second requirement for human missions at the Moon or Mars is to land within 50 m (±3 standard deviations or 3σ of a Gaussian distribution) of the landing target for the vehicle. These two requirements establish the precision landing criteria. Additional requirements exist to ensure vehicle safety, which is also referred to as hazard avoidance. The precision landing and hazard avoidance criteria assumptions used in this study are provided in Table 1 and include limitations on vehicle velocity and attitude and landing slope limitations. Actual landing criteria will be mission dependent.

Landing criteria are not the only considerations. During entry and descent there are several other constraints on the trajectory for crewed or autonomous systems and sensors to operate properly. The constraints include viewing angles needed for sensor data acquisition, time to process data or images, as well as time to make and execute a divert maneuver. The constraints throughout the trajectory form an acceptable precision landing flight corridor. While waypoints along that corridor have been identified for lunar and Mars missions, the specific waypoint and dispersions

along the corridor are mission and vehicle dependent. Sample trajectory corridor targets and elements are provided in Table 2.

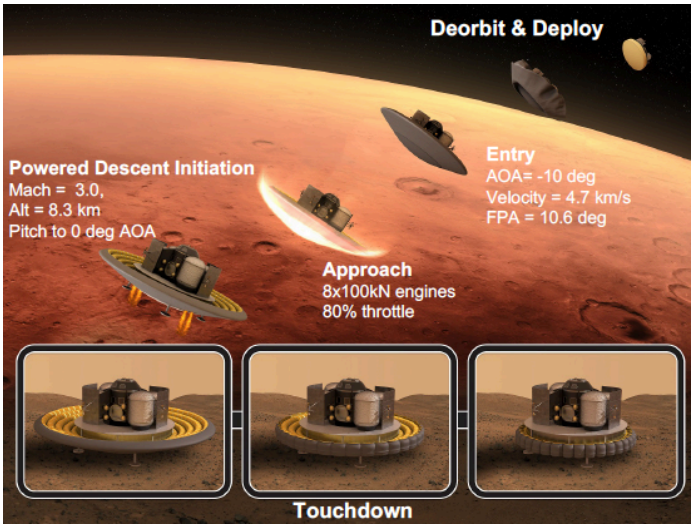

Fig. 1 Low L/D vehicle EDL concept of operations [2].

Table 1. Precision landing and hazard avoidance criteria.

Parameter	Value
Position Error from target	50 m
Horizontal Velocity	< 1.0 m/s
Vertical Velocities	< 2.0 m/s
Attitude	+/- 6 deg
Attitude rates	2 deg/s (all axes)

Table 2. Sample trajectory corridor targets, elements and considerations.

Trajectory Target	Elements	Consideration
Pre-Deorbit insertion burn	Position, Velocity	Number of orbits needed to obtain sufficient state knowledge
Post-Deorbit insertion burn	Position, velocity, attitude, attitude rate	Error propagation during the coast phase can be minutes to hours
Atmosphere Interface (Mars)	Velocity, attitude, attitude rate, range to target	Atmosphere dispersions and aerodynamic effects
Powered descent initiation	Altitude, velocity, attitude, attitude rate, range to target	Time dependent vehicle attitude change before and after engine initiation
Approach Phase	Altitude, velocity, attitude, attitude rate, range to target, range rate	Sensor operational constraints
Vertical Descent Phase	Altitude, velocity, attitude, attitude rate, range to target, range rate	Surface plume interaction effects

III. High Fidelity Simulation

To date, most human Mars EDL concept studies were performed using only three degree-of-freedom (DOF) simulations that assumed perfect navigation [2,4]. However, characterizing sensor performance for precision landing requires a higher fidelity six DOF simulation capability. The requirement to evaluate many concepts of operations necessitated a flexible simulation framework. The SPLICE high-fidelity simulation framework uses at its core the Program to Simulate Optimized Trajectories II (POST2) [5]. POST2 is an event-driven, point-mass trajectory simulation software with discrete parameter targeting and optimization capability. It provides multiple degrees-of-freedom simulation and assessment of endo-and exo-atmospheric trajectories about a planetary body. POST2 has

served as the primary EDL simulation for several recent Mars robotic missions including Mars Science Laboratory and InSight and is the prime simulation for the Mars 2020 EDL mission. Therefore, the SPLICE team leverages many of the relative and inertial navigation sensor implementation lessons learned from robotic missions for this effort.

Additionally, the POST2 code is modular, allowing for straight forward implementation of various vehicle parameters and models. The input format allows for standard vehicle parameters and trajectory way points to accommodate many types of concepts of operations. These features create a framework that allow for rapid model implementation and make the simulation flexible to accommodate various vehicles and concepts of operations. This section will summarize the guidance methodology for developing trajectories and will provide a detailed description of the navigation filter and sensor models incorporated in the simulation.

A. Guidance Methodology

Mars entry, descent, and landing (EDL) guidance strategies utilizing bank reversals and mass jettisons were successfully demonstrated during the Mars Science Laboratory mission in 2012 [6,7]. To achieve required performance and precision landing capabilities, future crewed Mars entry vehicles will require EDL guidance strategies that go beyond extensions of heritage approaches. Recent work has shown that significant improvement to landing performance for missions of this scale are achieved using an advanced numerical predictor-corrector guidance and direct force control (DFC) methods, which permit uncoupled management of parameters such as crossrange and downrange errors [8,9]. Therefore, the study considers an entry guidance approach for the low lift-to-drag (L/D) vehicle that achieves direct control of angle of attack (to control downrange) and side slip (to control crossrange). The method by which the vehicle achieves the control authority (e.g., using movable mass, articulating aerodynamic surfaces or changing the shape during flight) is not relevant to character navigation performance, but is discussed in detail in Ref [8].

B. Sensor Model Descriptions

The sensor models incorporated in the POST2 simulations include Terrain Relative Navigation (TRN), Hazard Detection (HD), an Inertial Measurement Unit (IMU), star tracker, altimeter velocimeter models, Navigation Doppler Light Detection and Ranging (LIDAR) and a flush air data system (FADS). At this point in the simulation development only behavioral sensor models are included. Behavioral models capture the sensor performance and timing by adding random noise and bias applied to truth data. Therefore, the behavior, or sensor performance, can be modeled without simulating full-fidelity physics that will be performed by the sensor hardware. These models will be upgraded as specific hardware and instruments mature. Alternative methods to implement and use the TRN model to autonomously track surface features are discussed elsewhere [10]. Finally, the navigation filter that processes and manages sensor data and mounting alignment errors are described.

The Navigation Filter: With the exception of the HD sensor, all models send data to the navigation filter. The HD model output is a set of safe landing sites, which are used by the guidance to target the final landing site. For sensors other than HD, the navigation filter blends the data from several sources to estimate the trajectory state of the spacecraft. A perfect navigation filter would output trajectory states equivalent to the truth states from the simulation. This perfect navigation filter assumption has been used in the analysis to date to gauge the performance of the guidance, controller, and actuators [2,4]; however, the perfect navigation assumption was initially replaced with an IMU-based propagation that leads to state estimates. The IMU propagated or dead-reckoned states are passed to the guidance, controller, and actuators. Now the navigation filter for the simulation is matured by modeling an Extended Kalman Filter (EKF) that blends output from various sensor types to generate the best estimate of the vehicle state and the state covariance matrix [11].

Inertial Measurement Unit: The IMU model was developed for Autonomous Landing Hazard Avoidance Technology (ALHAT) project. The IMU model was implemented in the POST2 end-to-end descent and landing simulation for the ALHAT Project [12] and used in several other POST2 mission simulations, including the Commercial Crew Program, Low-Density Supersonic Decelerator (LDSD)[13], Advanced Supersonic Parachute Inflation Research Experiments (ASPIRE) [14] and Adaptable Deployable Entry and Placement Technology (ADEPT) [15] flight test simulations. The IMU sensor is modeled as a strapdown or rigidly attached IMU located at a fixed point on the spacecraft. The IMU is assumed, but not required, to be at the vehicle's center of gravity. The sensor inputs are true sensed accelerations and attitude rates. The sensor outputs are acceleration and body rates with errors. This sensor is operational through the entire flight from deorbit to touchdown and the outputs are considered valid throughout the flight. Sensor errors include bias, noise, scale factor, misalignment, mounting errors and quantization errors. The errors are parameterized to model an IMU with many types of typical errors observed in IMU hardware; these parameters

are listed in Table 3. A complete description of the IMU error model is provided in Ref [16]. The IMU errors in Table 3 are based on representative existing hardware that are classified by their apparent quality; however, it is noted that the error quantities listed in Table 3 do not consistently change with improved quality in all parameters because some are based on existing hardware.

Table 3. IMU sensor measurement performance quality. All values are ±3σ (Gaussian).

Error	Low	Medium	High
Accel random walk	105 micro-g	150 micro-g	30 micro-g
Accel Bias (micro-g)	900	300	84
Accel Scale Factor (ppm)	900	525	450
Accel Non-ortho (arcsec)	20	45	17
Gyro random walk (deg/sqrt(hr))	0.21	0.018	0.015
Gyro Bias (deg/hr)	0.3	0.15	0.036
Gyro Scale Factor (ppm)	100	15	27
Non-orthogonality (arcsec)	60	75	19
Quantization	6.104e-05 m/s, 0.000109 deg		

Star Tracker: A behavioral model of the star tracker is implemented in the simulation. The model is not a physics-based model and does not take into account the ephemeris of stars and interplanetary position of the spacecraft. Rather the true attitude of the spacecraft between the inertial and body frame is an input into the model, and the model outputs attitude with noise and misalignment errors (shown in Table 4) superimposed on the input. The vehicle body frame has its origin at the vehicle's center of gravity. The x-axis is directed forward along the longitudinal axis along the apex, or nose of the vehicle. An image of the body coordinate frame is shown in Fig. 2. This sensor is operated every 10 seconds prior to atmosphere interface or powered descent initiation at bodies without an atmosphere. The model operation assumes a stable spacecraft configuration and is not used during RCS burns. Currently, fuel slosh effects and other vehicle vibrations are not considered in the validity model of the sensor.

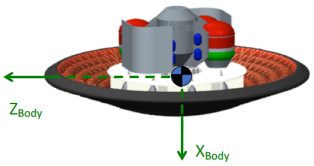

Fig. 2 Body axis definition.

Table 4. Star Tracker sensor measurement errors. All values are ±3σ (Gaussian).

Error	Low	Medium	High
Boresight Noise (arcsec)	207	68.2	24
Cross-sight Noise (arcsec)	49	8.2	3
Internal Misalignment	12 arcsec	10 arcsec	8 arcsec

Altimeter/Velocimeter: The behavioral altimeter and velocimeter models need inputs of the true altitude and planet-relative velocity in the vehicle body frame. The model output provides altitude above the surface and planet-relative velocity with errors. These sensors are based on heritage hardware like that found on Mars robotic missions, such as Mars Pathfinder, Mars Exploration Rovers, Phoenix, Insight, and Mars Science Laboratory, and are assumed to operate at higher starting altitudes than the Navigational Doppler Lidar (NDL) described in the next section. The operational envelope for this model includes altitudes up to 20 km down through powered descent initiation (in vacuum or atmosphere). At lower altitudes, only the NDL will be used to obtain altitude and velocity information. The purpose of including these sensors is to compare the navigation knowledge available at different points in the trajectory to the use of ground based (Earth or destination) communication assets and higher fidelity onboard assets like NDL. Error sources include random noise, scale factor and bias and are similar to those provided for NDL in the next section.

Navigational Doppler Light Detection and Ranging (LIDAR) or NDL: The NDL model implemented in the POST2 simulation is a behavioral model with rudimentary physics of doppler shift captured to inform the validity model. The NDL sensor includes three laser beams. Inputs to the model include true beam slant range to the ground, vehicle

attitude rates and velocity. The simulation can calculate the true beam slant range between the vehicle and digital elevation map (DEM), using ray-tracing methods that have been tested using the MSL and Mars 2020 mission simulations [17]. The model output includes line-of-sight range and velocity from each beam with errors as well as parameter indicating the validity of each beam measurement. Sensor errors include random noise, bias, scale factor and beam to beam misalignments. Sensor errors corresponding to various performance qualities for range and velocity are shown in Table 5 and Table 6 respectively. The quantities apply to each of the instrument's three beams along the line-of-sight (LOS). The maximum LOS velocity is 218 m/s. A low-quality measurement is characterized by the return of one beam, while higher quality measurements would include two beams or three beams that return data. Current work has not characterized packaging or placement of the NDL instrumentation within the confines of the spacecraft. Instead, the LIDAR is assumed to be mounted at the vehicle center of gravity and it is assumed that it can point in the nadir direction without obstruction from any engine effluent. Figure 3 shows the definition of slant range.

Table 5. NDL Range measurement performance quality. All values are ±3σ (Gaussian).

Error	Low	Medium	High
Noise (m)	6.6	6.6	6.6
Bias (cm)	60	60	60
Scale Factor (ppm)	$3.3\text{x}10^{-4}$ x Range	$3.3\text{x}10^{-4}$ x Range	$3.3\text{x}10^{-4}$ x Range
Single Beam Internal Misalignment (deg)	0.05	0.05	0.05
Beam to beam misalignment relative to optical bench (deg)	0.05	0.05	0.05
Min/Max range based on surface albedo	Moon: 30m to 5.5 km	10m to 6.5 km	5m to 7.5 km
	Mars: 30m to 4.5 km	10m to 5.5 km	5m to 6.0 km

Table 6. NDL Velocity measurement performance quality. All values are ±3σ (Gaussian).

Error	Low	Medium	High
Noise (cm/s)	5.1	5.1	5.1
Bias (mm/s)	3	3	3
Scale Factor (ppm)	$3\text{x}10^{-5}$ x Range	$3\text{x}10^{-5}$ x Range	$3\text{x}10^{-5}$ x Range
Internal Misalignment	0.05	0.05	0.05
Min/Max range based on surface albedo	Moon: 30m to 5.5 km	10m to 6.5 km	5m to 7.5 km
	Mars: 30m to 4.5 km	10m to 5.5 km	5m to 6.0 km

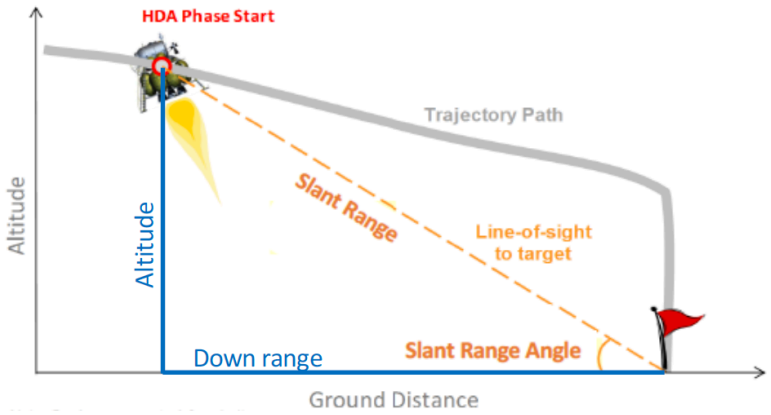

Fig. 3 Definition of slant range and slant range angle.

Terrain Relative Navigation (TRN): The TRN system performs surface feature tracking using camera images to provide position estimates. The camera obtains a visible spectrum descent image. On board software allows for feature recognition and extraction. Each image is compared with a reference image for feature-landmark pairing. Finally, the

software algorithm makes an estimate of the vehicle position. At present, the EDL simulation uses a simplified state space TRN model that relies on an explicit relationship between position accuracy and hardware parameters with heritage from the Mars 2020 Lander Vision System. The true lander state relative to a surface frame is input to the model and a position estimate relative to the surface is output. The model is assumed to operate in the altitude range between 6 km down to 1.5 km. The camera is assumed to point nadir.

Although current simulation results utilize a simplified TRN model, two different TRN model fidelities are available. The low-fidelity mode generates a position estimate that is equal to the true position plus a bias and noise term. The noise term is based on a least squares error covariance of a nadir pointing single image TRN system. On the other hand, the mid-fidelity model contains additional fidelity in the form of an internal Extended Kalman Filter (EKF) which uses multiple, sequential data arrays representing artificial landmarks within the field of view of the camera to update the state estimate produced by the TRN system. Local perturbations, outlier errors, and map quantization errors are added to the landmark map. The map quantization errors model the resolution of the reference map. Since the feature matching is done in discrete space, the position accuracy of the reference features is limited by the resolution of the reference map. The position estimation is made using multiple landmarks from multiple images. Due to the use of an EKF, the position estimation error is correlated in time. Figure 4 shows the conceptual difference between the low and mid fidelity TRN models, where the *C* frame is the camera frame, the *S* frame is the North, West, Up frame centered at the intended landing point and the index *k* in Fig. 4 represents the EKF update index. Since the model processes one landmark array at a time, *k* is also equal to the number of landmark arrays processed by the TRN system. Table 7 contains the TRN measurement performance quality parameters.

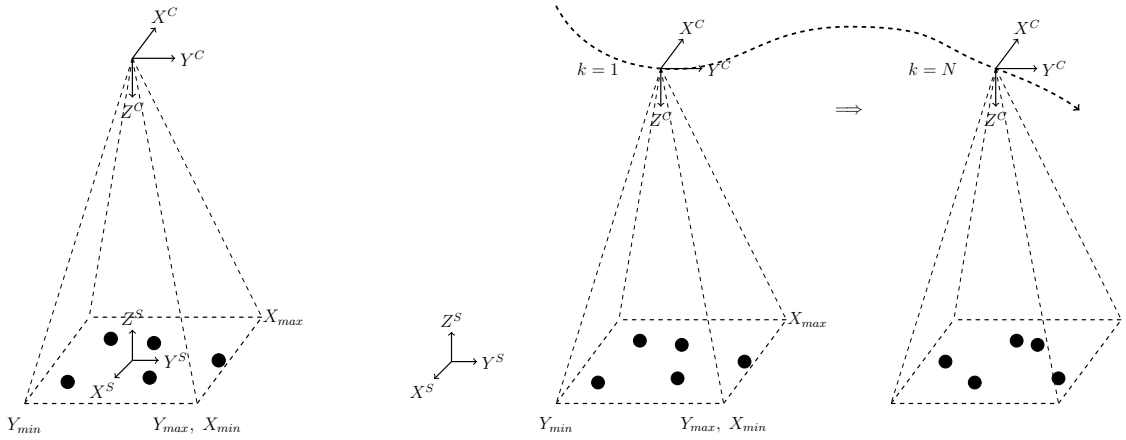

Fig. 4 Low (left) and Mid Fidelity (right) TRN model depictions.

Table 7. TRN sensor measurement performance quality. All values are ±3σ (Gaussian).

Error	Low	Medium	High
Horizontal Noise Range (m)	55 to 28	40 to 20	30 to 15
Vertical Noise Range (m)	80 to 40	50 to 25	40 to 20
Bias (m)	50	25	5

An example of the difference between the low and mid fidelity TRN, the simulation was run for each and the Root Sum Square (RSS) of the position error was calculated and plotted in Fig. 5 where position accuracy is shown as a function of lander altitude. While the low-fidelity model shows a monotonically decreasing error in position, the mid-fidelity model captures the realism of the EKF updates where the state estimate is corrected and the increase in error due to propagation error in between the state update states. Both models capture the changes in position accuracy as a function of lander altitude. The right plot of Fig. 5 is the result of a 600-trial Monte Carlo simulation. The matching ensemble and filter statistics indicate the mid-fidelity model is implemented correctly. The mid-fidelity model has improved performance due to the use of EKF and multiple updates. The increase in RSS bound between updates is due to velocity uncertainty [18].

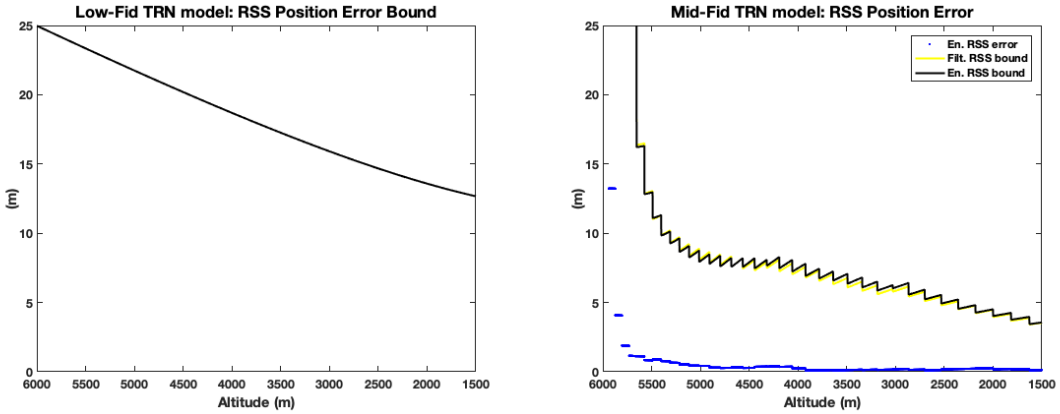

Fig. 5 Low fidelity (left) and mid (right) TRN model RSS position error bounds.

Hazard Detection (HD) System: Similar to the TRN, multiple sensors and onboard processing are necessary to generate HD output. Like the other models described so far, the HD model is behavioral in nature. The model takes as input the true and estimated lander state relative to the surface that is defined by a digital elevation map (DEM). Unlike the other models being considered, HD is the only one that does not provide input to the navigation filter; instead, it outputs a list of safe landing locations from which the guidance can choose. The general process for determining the list of safe sites is shown in Fig. 6. A LIDAR-derived DEM that the HD hardware would produce is simulated based on a true DEM and the model of the flash LIDAR. Using the LIDAR-based DEM, the HD algorithm generates a list of safe sites that meet the criteria of the safe map. The operational envelope of this instrument is fairly close to the surface, at an altitude of approximately 500 m.

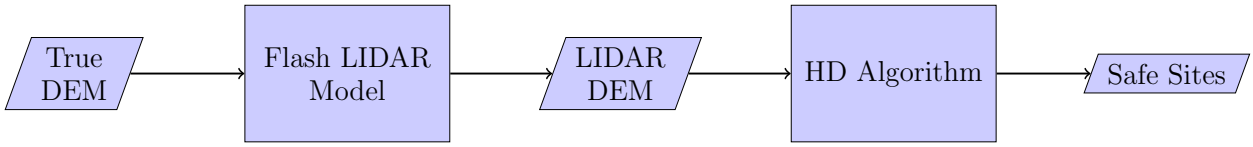

Fig. 6 Process for generating the list of safe sites in the Hazard Detection model.

Like the TRN, both a low and mid fidelity HD model are available in the simulation. The low fidelity behavioral model precomputes the safe landing locations using an independent and offline hazard detection simulation. A table of the safe spots for different lander sizes and DEM elevation uncertainties are supplied to the simulation. The mid-fidelity model includes a more mature LIDAR model and a previously developed ALHAT HD algorithm. The algorithm generates an estimated DEM that is processed by the HD algorithm to find safe sites. The HD algorithm uses the LIDAR DEM, the lander geometry, slope tolerance, roughness tolerance, and the navigation uncertainty to predict the probability of safe landing within the mapped region at 1-m resolution. Following the construction of the safety map, the algorithm selects aim points for guidance by searching for the peaks on the safety map [19]. For the mid fidelity HD model, the LIDAR position and orientation relative to the lander body frame as well as the detector field-of-view affect the final LIDAR field-of-view. The true DEM map of the terrain is shown in the left of Fig. 7. Then the estimated lander state is used together with the LIDAR ranges obtained using ray-intercept technique to form an LIDAR DEM which captures a region of the true DEM map. This image is shown in the middle of Fig.7. Finally, the HD algorithm calculates safety probability using LIDAR DEM map and generates a safety map that contains green areas of safe landing zones and identifies five specific locations with the highest probability of landing safety. This image is shown in the right of Fig. 7. The safe landing points are not input to the navigation filter but provided to the guidance algorithm to select the landing site.

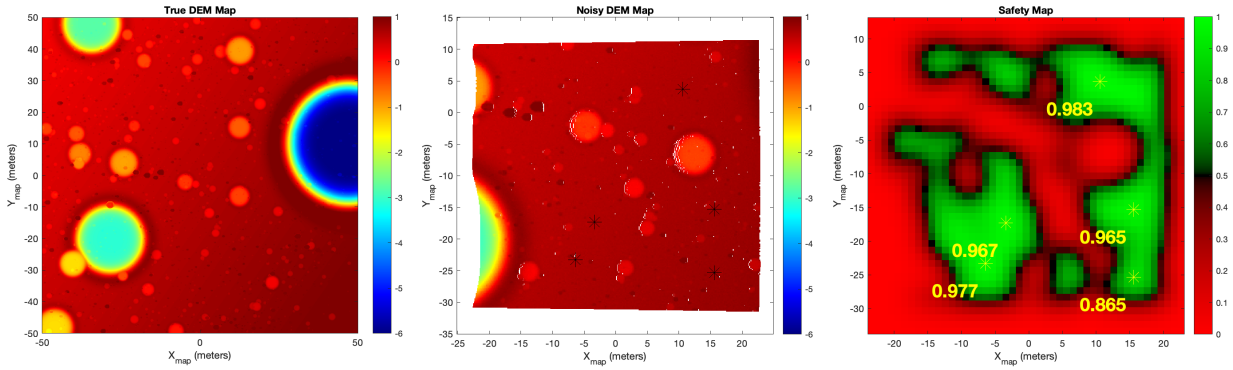

Fig. 7 True DEM map (left); LIDAR DEM map (middle); Safety map (right).

TRN and HD are designed for very different phases of the trajectory. TRN occurs higher in altitude when the vehicle has a large horizontal velocity. HD typically occurs when the vehicle has almost no horizontal velocity and is moving vertically toward the surface above the landing site. An image of the differences between TRN and HD is shown in Fig. 8. Determining the capability of both sensors to take adequate measurements for a wide range of precision landing trajectories is a key objective of the sensor evaluation. A summary of the next generation of hazard detection system development is summarized in [20].

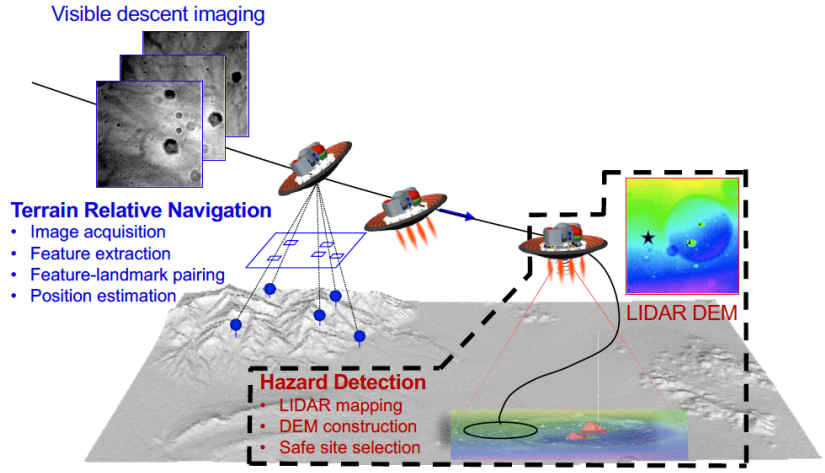

Fig. 8 TRN and HD operational modes.

Earth Update – Deep Space Network (DSN): Like other models, the Earth based updates sensor models are behavioral and do not take into account the ephemeris of the Earth or interplanetary position of the spacecraft. The model input includes true inertial position and the velocity of the spacecraft. Model outputs include the same quantities with errors associated with random noise. Table 8 shows the assumed navigation position and velocity error as the number of orbits and/or station data available prior to performing the deorbit burn [21]. Sensitivity studies using this model can influence mission architectural decisions and must be balanced with the reality of earth-based operations and multiple missions requiring DSN capabilities. The errors associated with DSN are characterized using the UVW frame. The UVW frame is defined as follows with respect to the landers inertial position (r) and velocity (v) vectors:

$$U = \mathbf{r}/|\mathbf{r}| \quad (1)$$

$$W = \mathbf{r} \times \mathbf{v} / |\mathbf{r} \times \mathbf{v}| \quad (2)$$

$$V = W \times U \quad (3)$$

Table 8. Earth Update – Deep Space Network performance quality. All values are ±3σ (Gaussian).

Error	Low	Medium	High
[U,V,W] position (km)	[0.9, 30.05, 3.07]	[0.15, 4.51, 0.61]	[0.03, 0.26, 0.21]
[U,V,W] velocity (m/s)	[28.54, 0.85, 0.15]	[4.57, 0.14, 0.03]	[0.24, 0.03, 0.01]

Flush Air Data System (FADS): The FADS system produces estimates of the freestream atmospheric state conditions by making measurements of the pressure distribution across the forebody and fitting them to a pressure model [22]. A FADS system was successfully flown as part of the Mars EDL Instrumentation (MEDLI) suite on the Mars Science Laboratory EDL mission [23] and is planned for the Mars 2020 mission. While MSL demonstrated the capability of the system at Mars and used the data to reconstruct the trajectory and validate models post flight, the intended use of a FADS system for precision landing is different. Notionally, the pressure and derived density data obtained during flight can be passed to the guidance and control systems to improve the knowledge state. A performance assessment was completed and summarized in Ref [22]. The FADS model is included as part of the SPLICE sensor suite to be evaluated at mission destinations with an appreciable atmosphere. Like other models being considered, the FADS model is a physics informed behavioral model. It uses a vehicle specific aerodynamic database derived pressure coefficient table that is a function of Mach number, dynamic pressure, angle of attack, sideslip angle, and instrument location on the forebody. The sensor input includes sensor location, true Mach number and dynamic pressure. Sensor errors include random noise and scale factor (see Table 9). The model outputs errors in angle of attack and sideslip. Due to current sensor limitations, the operational envelop includes the hypersonic to low supersonic flow regime. This sensor is not used for lunar applications. Even though the noise and scale factor are identical for each port, increasing the number of ports provides a more accurate measurement.

Table 9. FADS performance quality. All values are ±3σ (Gaussian).

Error	Low – 3 pressure ports	Medium – 5 pressure ports	High - 10 pressure ports
Noise (Pa)	5	5	5
Scale factor	0.5	0.5	0.5

Other Models: One of the other models being considered for the sensor assessment but not yet implemented is a Terrain Camera, or optical navigation camera, capable of detecting and characterizing craters at higher altitudes than the TRN model described herein. A second model being considered is ground beacons. These are assumed to provide Electra-like [24] state updates providing relative spacecraft position and velocity with respect to known preplaced surface assets at the mission destination. Finally, models of orbiting beacons are also being considered in the suite. These sensors would provide relative spacecraft position and velocity with respect to known states of the orbiting asset. While not currently being modeled, these sensors provide alternatives in the event that onboard sensor options cannot meet landing requirements.

Mounting Errors: All of the errors covered to this point are internal to the respective sensors. Additional error is associated with the location/orientation of the sensor with respect to the navigational filter assumptions. It is noted that there is a physical limitation that a specific sensor cannot be mounted to better than a 0.001m error without adding cost to the assembly. Table 10 provides the errors in position and orientation for poor and tight mount assumed in the sensor assessment.

Table 10. Mounting errors. All values ±3σ (Gaussian).

Error	Poor Mount	Medium	Tight Mount
Position (m) in [x,y,z]	0.005	0.001	0.001
Orientation (boresight) (deg)	0.25	0.1	0.05

A note regarding vehicle accommodation. The assumption is made that all sensors are located at the vehicle center of gravity in order to perform the initial sensor assessment. Considering the vehicle configuration shown in Fig. 2, that is not realistic or feasible. The first priority of the assessment is to determine which sensor combinations are

needed at various destinations to achieve precision landing. Future work will include vehicle specific details, account for displacement from the center of gravity, and assess sensor accommodation though all phases of flight, especially powered descent where the sensor could be obstructed by engine plume and near touchdown when the engine plumes interact with the surface regolith.

IV. Results

In the POST2 simulation, the EKF was activated at entry interface (EI). Also, the star tracker and DSN updates occur at EI. These are not realistic assumptions given that the navigation filter would be running during the parking orbit, deorbit, and coast to entry interface, and DSN and star tracker updates would occur prior to EI. However, it was sufficient to demonstrate the overall sensor suite in the simulation. The IMU was active starting at EI and operated through to landing. The TRN was active between altitudes of 1.5 km and 6.0 km. Several Monte Carlo simulations consisting of 8001 cases were run. Each Monte Carlo considered a different combination of sensor suites. A single random dispersed trajectory from each Monte Carlo was selected for the following analysis.

Figure 9 shows the navigation position error from 120 km altitude to touchdown (left) and an expanded view from 6 km to touchdown (right) for several different simulated trajectories. The navigation position error is difference between the square root of the sum of the squares of x-y-z inertial navigated state and truth position. The first trajectory assumes only a perfect IMU (no noise, bias, scale factor, or misalignment errors) with measurement quantization is used as the only navigation sensor (denoted in Fig. 9 as *Perfect IMU*). It can be seen that even with a perfect IMU with quantization, the final navigation error is approximately 75 m due to continuous integration and pointing errors. It is noted that navigation errors depend on the length of the flight and the sensor measurement frequency, which are assumed to be the same in all cases presented here. Studies to evaluate optimal sensor measurement frequency are not included.

The second trajectory replaces the perfect IMU with the high-quality IMU with quantization (as defined in Table 3) (denoted in Fig. 9 as *Hi IMU*). In this case, the navigation error at touchdown increases only slightly, though this is misleading as this is a single dispersed case (Fig. 10 will present these results in a statistical sense). This highlights the need to have sensors that update the navigated states and complement the integrated IMU.

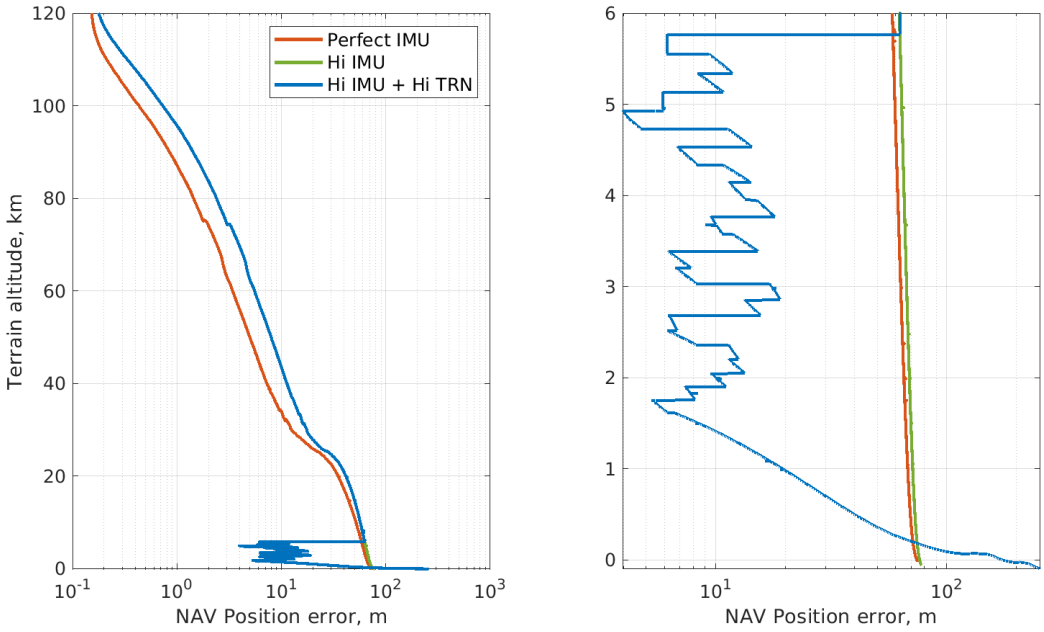

Fig. 9 Navigation position errors with various sensor suites, one random case selected from 8001-case Monte Carlo runs.

The third trajectory assumes a high-quality IMU with quantization and a high-quality TRN was run as part of the sensor suite (denoted *Hi IMU + Hi TRN*). The high-quality TRN was activated at 6 km and deactivated at 1.5 km per the TRN sensor specifications. In this case, the navigation error at TRN initiation immediately dropped from over 60

m to approximately 10 m and stayed at this magnitude until the TRN was deactivated at an altitude of 1.5 km. At this point, the navigation error slowly increased to 250 m at touchdown. The increase in position error after TRN is turned off is likely due to velocity uncertainty. These analyses did not consider a velocimeter. If velocity errors can be reduced through the use of a velocimeter, then the increase in position error after the TRN is turned off can also be reduced. Position error could also be reduced with further navigation filter tuning and additional sensors. Beyond the performance of individual trajectories, Fig. 10 shows the histograms for the same Monte Carlo cases. Table 11 lists the relevant statistics. From the plots and the table, it can be seen that the perfect IMU case has a relatively small NAV position error distribution, though they are biased by approximately 77 m. The high-quality IMU case has a significantly larger spread with a correspondingly higher mean error due to noise, bias, scale factor, and misalignment error propegation. Finally, it can be seen that the high-quality IMU with high-quality TRN case helps bring these navigation errors back down (smaller distribution), though a bias still exists. These results represent preliminary analyses and emphasize the need to include additional sensors updates to the navigation filter during the terminal phase of flight. An evaluation of the performance of all sensors presented in this paper is on-going.

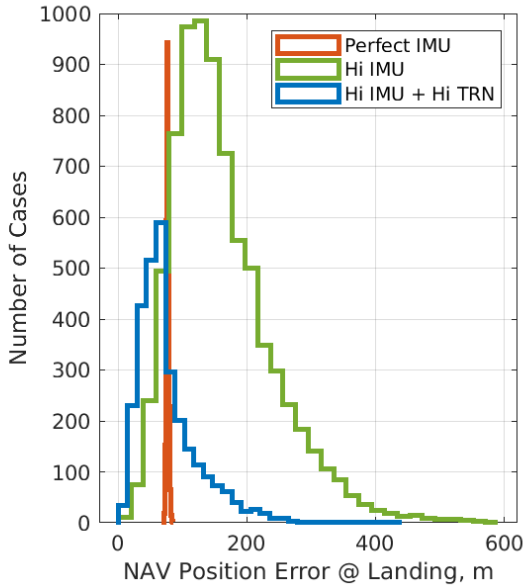

Fig. 10 Histograms, navigation position error with various sensor suites, 8001-case Monte Carlo runs.

Table 11 Statistics, navigation position errors with various sensor suites, 8001-case Monte Carlo runs.

	Mean (m)	99%-tile (m)
Perfect IMU	76.7	81.4
Hi IMU	161.6	410.7
Hi IMU + Hi TRN	76.3	230.6

V. Trades and Sensitivities

Specific trades and sensitivity studies will be driven by further analysis of the Monte Carlo simulations results presented in Section IV. As the initial results indicated, using the high-fidelity sensors within the sensor defined operation limits resulted in almost 250 m position error at touch down (Fig. 9 Hi IMU + Hi TRN) and exceed the desired 50m position error. However, in addition to position error, other landing criteria, from Table 1 need to be analyzed (e.g., velocity, attitude, and attitude rates). Likewise, prior to including hazard detection, other analyses can be made to fully evaluate the initial sensor set. First, efforts are needed to tune the guidance algorithm and navigation filter to optimize performance. Second, modifications to the trajectory geometry can be considered to improve sensor performance. Based on the results of the characterization of the high-quality sensor suites, follow on studies will focus on obtaining data earlier in the trajectory, using an altimeter and/or velocimeter at altitudes above the 6 km TRN limit need to be explored. Then orbiting and surface beacons can be added as needed to meet precision landing constraints. Extensive trades may be needed to determine the number and location of the beacons. The beacon study adds a

dimension to the analysis. It moves beyond vehicle specific trades into architecture level trades. Besides sensor performance, other metrics that impact vehicle design are of interests such as total propellant used and conditions at engine initiation (especially Mach and flight path angle for the human Mars trajectories).

Once optimal and successful precision landing trajectories are identified, hazard detection can be incorporate along with sensor quality trades. Eventually sensor vehicle accommodation can be considered. It is noted that these trades are applied to a human Mars low L/D vehicle concept of operations. The POST2 simulation framework has been designed to be flexible to incorporate many vehicle descriptions and landing destinations. While near term work will focus on characterizing human lunar and Mars concepts of operations, notionally, the simulation can support precision landing and hazard avoidance sensor characterization for a wide range of concepts of operation and mission types, both robotic and human scale. As of publication, these trades have just begun and will be the focus of follow-on efforts.

VI. Conclusion

To meet NASA's challenge to return humans to the Moon in 2024 and establish a sustainable presence in 2028 requires advances in autonomous spacecraft navigation. This paper summarizes the simulation framework being developed to evaluate the navigation sensor performance that will enable precision landing and autonomous navigation for a variety of concepts of operations, including human lunar missions. This paper summarized the sensor models currently being incorporated in the simulation and presented initial sensor suite combination results. The results will guide detailed trade and sensitivity analyses for precision landing in the upcoming year. While the simulation framework and analysis capabilities being developed to evaluate various sensor combinations and mission concepts will inform technology investments and mission design, the ultimate goal of the task it to identify sensor or sensor suite commonalities that exist across destinations and mission type. Those sensor suites become technology investment recommendations that will affect both near- and long-term missions.

Acknowledgments

The authors would like to acknowledge others whose work was instrumental in developing, implementing and validating the models in the precision landing and hazard avoidance high fidelity performance simulation. They include Scott Striepe, John Carson, Ron Sostaric, David Woffinden, James McCabe, Chris Karlgaard, Richard Powell, George Chen, Farzin Amzajerdian, Glen Hines, Diego Pierrottet, Carolina Restrepo, and Jake Tynis.

References

[1] Cianciolo, A. D., Striepe, S., Carson, J., Sostaric, R., Woffinden, D., Karlgaard, C., Lugo, R., Powell, R., and Tynis, J. "Defining Navigation Requirements for Future Precision Lander Missions." AIAA 2019-0661.

[2] Cianciolo, A. D., Dillman, R., Brune, Lugo, R. A., Polsgrove, T. T., Percy T. K., Sutherlin, S., A., Johnson, C., and Cassell, A., "Human Mars Entry, Descent and Landing Architecture Study: Deployable Decelerators," AIAA Paper 2018-5191, Sept. 2018.

[3] Liever, P. A., Gale, M. P., Mehta, R. S., West, J. S. "Gas-Granular Simulation Framework for Spacecraft Landing Plume-Surface Interaction and Debris Transport Analysis." M18-6484, 2018.

[4] Polsgrove, T. T., Percy, T. K., Garcia, J., Cianciolo, A. D. Samareh, J., Lugo, R., Robertson, E., Cerimele, C., Sostaric, R., and Garcia, J., "Human Mars Entry, Descent and Landing Architecture Study: Rigid Decelerators," AIAA 2018-5191.

[5] Lugo, R. A., Shidner, J. D., Powell, R. W., Marsh, S. M., Hoffman, J. A., Litton, D. K., and Schmitt, T. L. "Launch Vehicle Ascent Trajectory Simulation using the Program to Optimize Simulated Trajectories II (POST2)," AAS Paper 17-274.

[6] Mendeck, G. M., and McGrew, L. C. "Post-Flight EDL Entry Guidance Performance of the 2011 Mars Science Laboratory Mission," AAS 13-419.

[7] Way, D. W., Davis, J. L. and Shidner, J. D. "Assessment of the Mars Science Laboratory Entry, Descent and Landing Simulation," AAS 13-420.

[8] Cianciolo, A. D., Korzun, A., Lugo, R. A., Slagel, A., Queen, E., Dillman, R., and Powell, R. "Low Lift-to-Drag Morphing Shape Design." AIAA SciTech 2020 Abstract Accepted.

[9] Lugo, R. A. and Powell, R. W. "Overview of a Generalized Numerical Predictor-Corrector Targeting Guidance with Application to Human-Scale Mars Entry, Descent, and Landing." AIAA SciTech 2020 Abstract Accepted.

[10] McCabe, J., and DeMars, K. J. "Anonymous Feature Processing for Efficient Onboard Navigation". AIAA SciTech 2020 Abstract Accepted.

[11] Murri, D., "Simulation Framework for Rapid Entry, Descent and Landing Analysis: Phase 2 Results." NASA TM-2011-217063

[12] Davis, J., Striepe, S., Maddock, R., Hines, G., Paschall, S., Cohanim, B., Fill, T., Johnson, M., Bishop, R., DeMars, K., Sostaric, R., and Johnson, A., "Advances in POST2 End-to-End Descent and Landing Simulation for the ALHAT Project," AIAA 2008-6938.

[13] Dutta, S., Bowes, A., White, J., Striepe, S., Queen, E., O'Farrell, C., and Ivanov, M., "Post-Flight Assessment of Low-Density Supersonic Decelerator Flight Dynamics Test 2 Simulation," AAS 16-222.

[14] Dutta, S., Queen, E., Bowes, A., Leyleck,E., and Ivanov, M., "ASPIRE Flight Mechanics Modeling and Post Flight Analysis," AIAA 2018-3625.

[15] Dutta, S. and Green, J. S., "Flight Mechanics Modeling and Post-Flight Analysis of ADEPT SR-1," AIAA 2019-2900.

[16] Karlgaard, C., Blanchard, R., Kirsch, M., Tartabini, P., and Toniolo, M., "Hyper-X Post-Flight Trajectory Reconstruction," Journal of Spacecraft and Rockets, Vol. 43, No. 1, 2006, pp. 105–115. doi:10.2514/1.12733.

[17]Shidner, J., "An efficient ray-tracing method for determining terrain intercepts in EDL simulations," 2016 IEEE Aerospace Conference, Big Sky, MT, 2016, pp. 1-9.

[18] Mourikis, A. I., Trawny, N., Roumeliotis, S. I., Johnson, A. E., Ansar, A., and Matthies, L. (2009). Vision-aided inertial navigation for spacecraft entry, descent, and landing. *IEEE Transactions on Robotics*, *25*(2), 264-280.

[19] Ivanov, T., Huertas, A., and Carson, J. M. (2013). Probabilistic hazard detection for autonomous safe landing. In *AIAA Guidance, Navigation, and Control (GNC) Conference* (p. 5019).

[20] Restrepo, C. I., Sostaric, R. R., and Carson, J. M. "Next Generation NASA Hazard Detection System Development." AIAA SciTech 2020 Abstract Accepted.

[21] Emil Schiesser, "CEV Navigation Sensor Suite Preliminary Design" Memo EG-CX-06-2 March 17, 2006.

[22] Lugo, R. A., Karlgaard, C.D., Powell, R. W. Cianciolo, A. D., "Integrated Flush air Data Sensing System Modeling for Planetary Entry Guidance with Directo Force Control." AIAA 2019-0663.

[23] Karlgaard, C. D., Kutty, P., Schoenenberger, M. Shidner, J., Munk, M. "Mars Entry Atmospheric Data System Trajectory Reconstruction Algorithm and Flight Results" AIAA 2013-0028.

[24] Schratz, B. C., Soriano, M., Ilott, P., Shidner, J., Chen, A., Bruvolk, K. "Telecommunications Performance During Entry, Descent, and Landing of the Mars Science Laboratory." Journal of Spacecraft and Rockets. Vol. 51, No. 4, July–August 2014.